RSC Advances

PAPER

Cite this: *RSC Adv.*, 2019, **9**, 24164

α-Fe_2O_3 hollow meso–microspheres grown on graphene sheets function as a promising counter electrode in dye-sensitized solar cells†

Guomin Zhao, * Guangji Xu and Shuang jin

Received 6th April 2019
Accepted 18th July 2019

DOI: 10.1039/c9ra02586c

rsc.li/rsc-advances

Although nanoparticles, nanorods, and nanosheets of α-Fe_2O_3 on graphene sheets have been synthesized, it remains a challenge to grow 3D α-Fe_2O_3 nanomaterials with more sophisticated compositions and structures on the graphene sheets. Herein, we demonstrate a facile solvothermal route under controlled conditions to successfully fabricate 3D α-Fe_2O_3 hollow meso–microspheres on the graphene sheets (α-Fe_2O_3/RGO HMM). Attributed to the combination of the catalytic features of α-Fe_2O_3 hollow meso–microspheres and the high conductivity of graphene, α-Fe_2O_3/RGO HMM exhibited promising electrocatalytic performance as a counter electrode in dye-sensitized solar cells (DSSCs). The DSSCs fabricated with α-Fe_2O_3 HMM displayed high power conversion efficiency of 7.28%, which is comparable with that of Pt (7.71%).

1. Introduction

Notably, mesoporous materials have exhibited many applications in the fields of catalysis, electron transfer, energy conversion and storage, owing to their tailored pore structures and high surface areas.[1–5] The interest in mesoporous α-Fe_2O_3 has strongly increased owing to its high resistance to corrosion, environment friendliness, magnetic behavior, and catalytic activity.[6–10] Currently, mesoporous α-Fe_2O_3 with regular morphologies, such as nanoparticles, nanorods, mesoporous films, mesoporous (hollow) microspheres, and mesoporous walls, have been successfully obtained by chemical and physical routes.[11–13] The investigation for mesoporous α-Fe_2O_3 microspheres revealed that these microspheres with sufficient thickness increase the reactive surface together with many active surface sites, effectually accommodating the volume expansion and enhancing the electronic conductivity.[14–16] These favorable structure features of the mesoporous α-Fe_2O_3 microspheres lead to promising properties for electrochemical applications.

Due to the unique two dimensional and layered-structure of sp^2-hybridized carbon atoms, graphene as a semiconductor possesses zero bandgap, owns novel electronic properties, and excellent abilities, such as electron storage and transport.[17–20] Recent studies have revealed that the growing or anchoring nanomaterials on graphene can greatly improve the catalytic performances of semiconductors and electrochemical performances of the electrode materials. For example, Zhang *et al.* fabricated the mesoporous $Ni_{0.85}Se$ nanospheres and NiSe–Ni_3Se_2 hollow hybrid nanostructure on graphene to obtain excellent electrocatalytic performance as counter electrodes of dye-sensitized solar cells.[21–24] Li *et al.* wrapped the mesoporous Fe_3O_4 in nitrogen-doped graphene networks to achieve remarkable electron-transfer ability and highly efficient electrocatalytic active sites.[25,26]

More recently, a few reports have demonstrated the great potential of the graphene composited α-Fe_2O_3 nanoproducts, including α-Fe_2O_3 nanoparticles, nanoplates, and nanorods in the applications of Li-ion batteries, photocatalysis, electrocatalysis, and supercapacitors.[27–30] Palermo *et al.* grew α-Fe_2O_3 nanowalls on the reduced graphene oxide (RGO) sheets to create complex hierarchical electrodes in the Li-ion batteries. They found that the new anode possessed a specific capacity of up to 1175 μA h cm^{-2} and capacity retention of 84% after 1000 cycles.[31] The investigation for the electrocatalytic properties revealed that Fe_2O_3 nanocrystalline/graphene oxide composites as electrocatalysts for the oxygen reduction reaction enhanced the onset potential, cathodic potential, and electrochemical stability.[32] Fang *et al.* fabricated α-Fe_2O_3 tetrakaidecahedrons on graphene oxide and demonstrated it to be efficient photoelectrodes for photoelectrochemical water splitting reaction with superior photocurrent response.[33] Unfortunately, even though nanoparticles, nanorods, and nanosheets on the graphene sheets have been synthesized, it remains a challenge to grow 3D nanomaterials, with more sophisticated compositions and structures, on graphene sheets.

Herein, we report the synthesis of α-Fe_2O_3 with a hollow meso–microsphere like morphology on the reduced graphene oxide (α-Fe_2O_3/RGO HMM) nanosheets through the solvothermal route. The decomposition of

School of Energy and Safety Engineering, Tianjin Chengjian University, Tianjin 300384, China. E-mail: guominzhao@163.com

† Electronic supplementary information (ESI) available. See DOI: 10.1039/c9ra02586c

hexamethylenetetramine at a temperature of 150 °C provided –OH at the rate of good diffusion, and the graphene oxide sheets were used as templates. The formation mechanisms of α-Fe_2O_3/RGO HMM were further investigated. Additionally, α-Fe_2O_3/RGO HMM was applied as the counter electrode (CE) of the dye-sensitized solar cell (DSSC) to analyze its electrocatalytic performance for the first time. Thus, benefiting from the favorable structural features of α-Fe_2O_3 HMM and the excellent electronic properties of graphene, α-Fe_2O_3/RGO HMM exhibited superior electrocatalytic performance for promising DSSCs.

2. Experimental section

Synthesis of α-Fe_2O_3/RGO HMM

The graphene oxide (GO) nanosheets were made by a modified Hummers' method. The concentration of the final GO water suspension was ~5 mg mL^{-1}. A two-step approach for the synthesis was used in this process. In the first step of the synthesis, 10 mL of GO water suspension was injected into a 50 mL beaker with 30 mL of water, and then 0.9 g of $FeCl_3 \cdot 6H_2O$ was added with magnetic stirring to form a homogeneous solution. Subsequently, the mixture was transferred into a Teflon-lined stainless-steel autoclave with a capacity of 50 mL for the hydrothermal treatment at 150 °C for 15 h. In the second step of the synthesis, after the autoclave was allowed to cool to room temperature, 0.3 g of hexamethylenetetramine and 0.2 g of L-ascorbic acid was added to the autoclave with magnetic stirring. The mixture was then sealed in the autoclave for the hydrothermal reaction at 150 °C for another 9 hours. The precipitate formed was separated by centrifugation and then washed with water and absolute ethanol to remove impurities. Eventually, the α-Fe_2O_3/reduced graphene oxide hybrid was obtained by drying.

Characterization

The phase of the samples was characterized by X-ray diffraction (XRD) under a Rigaku D/Max-2500 X-ray diffractometer, employing Cu Kα radiation, $\lambda = 1.54056$ Å. The morphology and the size of the samples were characterized by using a field emission scanning electron microscope (JEOL JSM-6700), transmission electron microscope (TEM, JEOL-2010, operating voltage of 200 kV), and high-resolution TEM (HR-TEM, JEOL-2010). Further, the elemental composition was detected by X-ray photoelectron spectroscopy (XPS, Kratos Axis Ultra DLD). The Brunauer–Emmett–Teller (BET) surface area was obtained on a Quanta-chrome NOVA 2000e sorption analyzer.

3. Results and discussion

Fig. 1a shows the X-ray diffraction (XRD) pattern of the synthesized products. It can be seen that the pattern conforms to rhombohedral α-Fe_2O_3 ($a = b = 5.038$, $c = 13.772$ Å, JCPDS Card No. 33-0664). However, no characteristic peaks were observed for other impurities such as γ-Fe_2O_3 and Fe_3O_4. Fig. 1b shows the N_2 adsorption/desorption isotherm and the pore-size distribution (inset) of α-Fe_2O_3/RGO HMM. The isotherms were identified as type IV, which are characteristic of the mesoporous materials. The pore-size distribution obtained from the isotherm indicates the presence of a number of pores, with the sizes being less than 3 nm in the samples. These pores presumably arise from the spaces among the nanoparticles. The sharp distribution of the mesopores around 3 nm suggests that the nanoparticles have good mono-dispersity. Furthermore, the large pores of around 12 nm were attributed to the interparticle spaces. The sharp distribution of the mesopores around 12 nm suggests that the NPs have high mono-dispersity. Further, the BET specific surface area of the sample was calculated from N_2 isotherms at −196.68 °C, and was found to be about 20.92 m^2 g^{-1}. The low-magnification field-emission scanning electron microscopy (FESEM) images indicate that the as-obtained α-Fe_2O_3/RGO HMM was composed of uniform spheres (Fig. 1c). The higher-magnification SEM images revealed that α-Fe_2O_3 microspheres, approximately 0.6 μm in size, were built from the nanoparticles (Fig. 1d). Indeed, the surface of the nanospheres was rough and consisted of many small particles that were assembled to form the spheres.

Further, the atomic force microscopy (AFM) image (Fig. 2a) indicates the height of the graphene oxides to be in the range of 0.35–1 nm, which revealed that the graphene oxide sheets were either mono- or bi-layered. The high-resolution TEM (HR-TEM) images (Fig. 2b and c) presented a typical image of α-Fe_2O_3 hollow meso–microsphere on an isolated graphene surface, in which the edge portions of the superstructures were thicker than that of the center and were composed of the nanoparticle-like 0D nanostructure. The image reveals that the lattice fringes extend over the entire particle, thus indicating that the entire particle is monocrystalline (Fig. 2d). Additionally, the distances between the adjacent lattice fringes, measured as 2.78 Å, were the interplanar distances of α-Fe_2O_3 (104) and are in excellent agreement with the literature value of the (104) d-spacing (JCPDS Card No. 33-0664).

The relationship between the shape of α-Fe_2O_3 and the synthesis time was also investigated. The synthesis time for α-Fe_2O_3/RGO HMM were 1, 2, 4, 8, and 15 h (before adding hexamethylenetetramine), and the corresponding TEM images are shown in Fig. 3a–e. Many rod-like and a few irregular particle-like products were formed on GO in the synthesis time of 1 h (Fig. 3a), and a clear rod-like morphology was formed on GO with a synthesis time of 2 h (Fig. 3b). As the reaction time was increased to 4 h, many rod-like and a few sphere-like shapes were formed on GO (Fig. 3c); the clearer spheres were formed in a synthesis time of 8 h (Fig. 3d), and the microspheres with narrowly distributed diameters were formed on GO in a reaction time of 15 h (Fig. 3e). After 15 h of reaction (in the absence of hexamethylenetetramine and Vc), hexamethylenetetramine and Vc were added and hydrothermally treated for another 1 h or 2 h (Fig. 3f and g), which in turn led to the formation of mesoporous microspheres with narrowly distributed diameters on RGO. The results reveal that the reaction time is one of the most important parameters in forming α-Fe_2O_3 mesoporous nanospheres on GO with narrowly distributed diameters, thereby indicating that the Ostwald ripening process is indispensable.

Based on the above observations, a growth evolution from initial irregular aggregations to final 3D hollow meso–

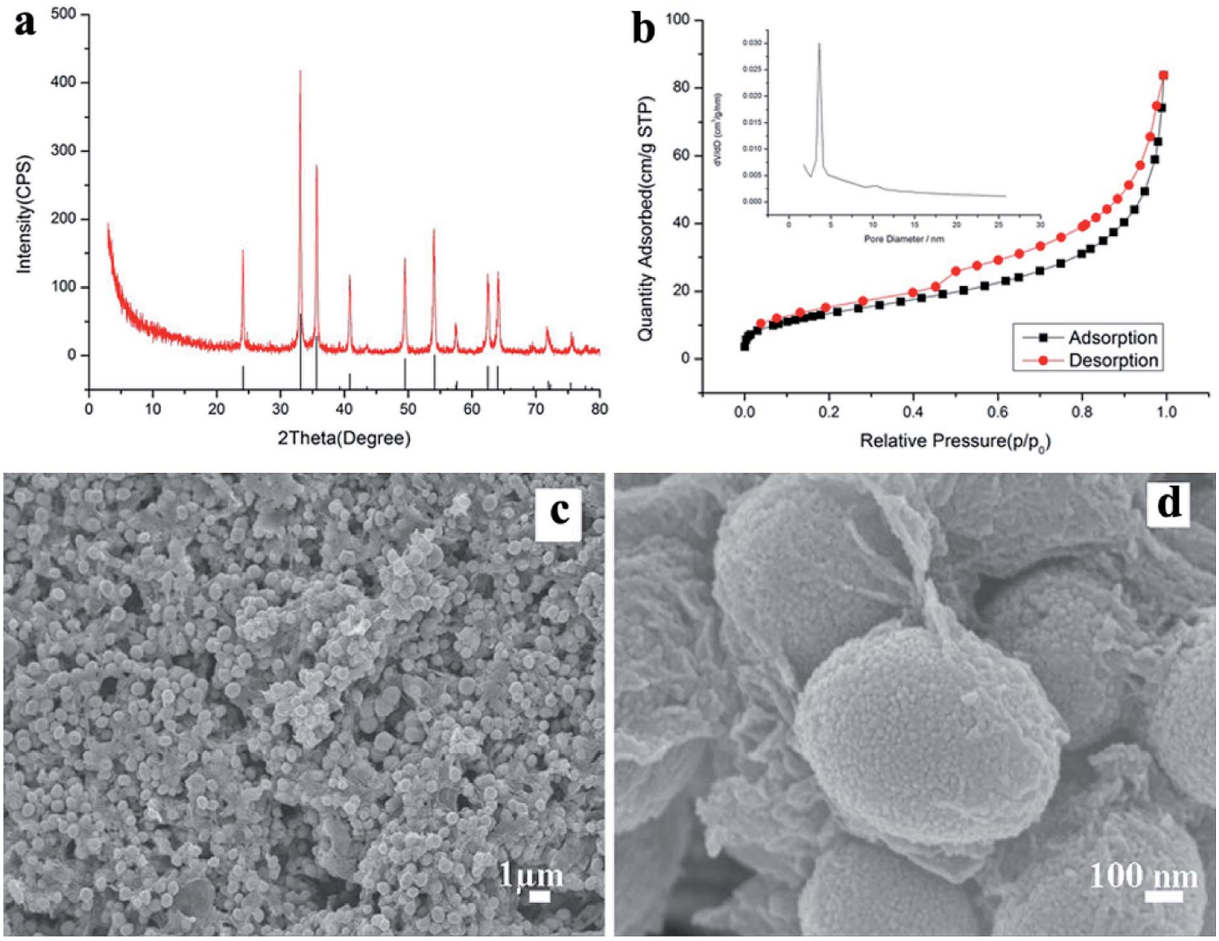

Fig. 1 The XRD pattern of prepared α-Fe_2O_3/RGO HMM (a); N_2 adsorption/desorption isotherm and the pore-size distribution (inset) of α-Fe_2O_3/RGO HMM (b); FESEM images of α-Fe_2O_3/RGO HMM: (c) low magnification, and (d) high magnification.

microspheres could be observed. It is well-known that there are –OH and –COOH functional groups on the surfaces of graphene oxides, which provide complex sites for cations.[34,35] Before the synthetic reaction occurs, a lot of Fe^{3+} ions gather on the complex sites, and subsequently, hydrolyze to form the FeOOH crystal nucleus, followed by the attachment of these instantaneously formed FeOOH nanoclusters in solution to the FeOOH nucleus on the complex sites. As a result, the cluster gathers into colloidal spherical aggregates to minimize their surface area and decrease their energy.[36] Due to anisotropy, the colloidal spherical structures aggregate to form nanorods. This can be further confirmed from Fig. 3b, in which the irregular aggregations, instead of rods, were the main products. This transition could be considered as a typical Ostwald ripening process, during which the small nanoparticles dissolved and redeposited onto the large crystals to form the long rods. With a further increase in the reaction time, there was a transition from rods to 3D hollow meso–microspheres. Therefore, we propose that the formation of rods was kinetically favorable, so they were the predominant products formed in the short reaction time. However, microspheres possess higher thermodynamic stability, so they were the predominant products formed in the long reaction time. As a result, the rods dissolved and recrystallized to form the spherical particles through the Ostwald ripening process, in which each spherical particle was produced by the aggregation of many nanoparticles. These spherical nanoparticles were well separated and had uniform size and shape, such as those shown in Fig. 1c and d.

To research the electrocatalytic property of the prepared α-Fe_2O_3/RGO HMM samples, EIS was performed with the symmetric cells. The Nyquist plots of α-Fe_2O_3/RGO HMM and Pt electrodes are illustrated in Fig. 4. The intercept of the real axis in the high-frequency region denotes the series resistance (R_s), and the diameter of high-frequency semicircle represents the charge transfer resistance (R_{ct}) of the electrolyte/electrode interface.[37] The values of R_s and R_{ct} were obtained by fitting the Nyquist plots and are listed in Table 1. The R_s value of α-Fe_2O_3/RGO HMM (12.72 Ω cm^2) was close to that of Pt CE (12.70 Ω cm^2), revealing its good conductivity and contact with the FTO substrates. It is well-known that the R_{ct} values in DSSCs exhibit significant influence on the short-current density and fill factor in the photocurrent–voltage curve.[38] Hence, owing to the fast charge transfer channels of the hollow-mesoporous nanostructure and the high conductivity of graphene, the R_{ct} value (2.32 Ω cm^2) of Fe_2O_3/RGO HMM was found to be very close to

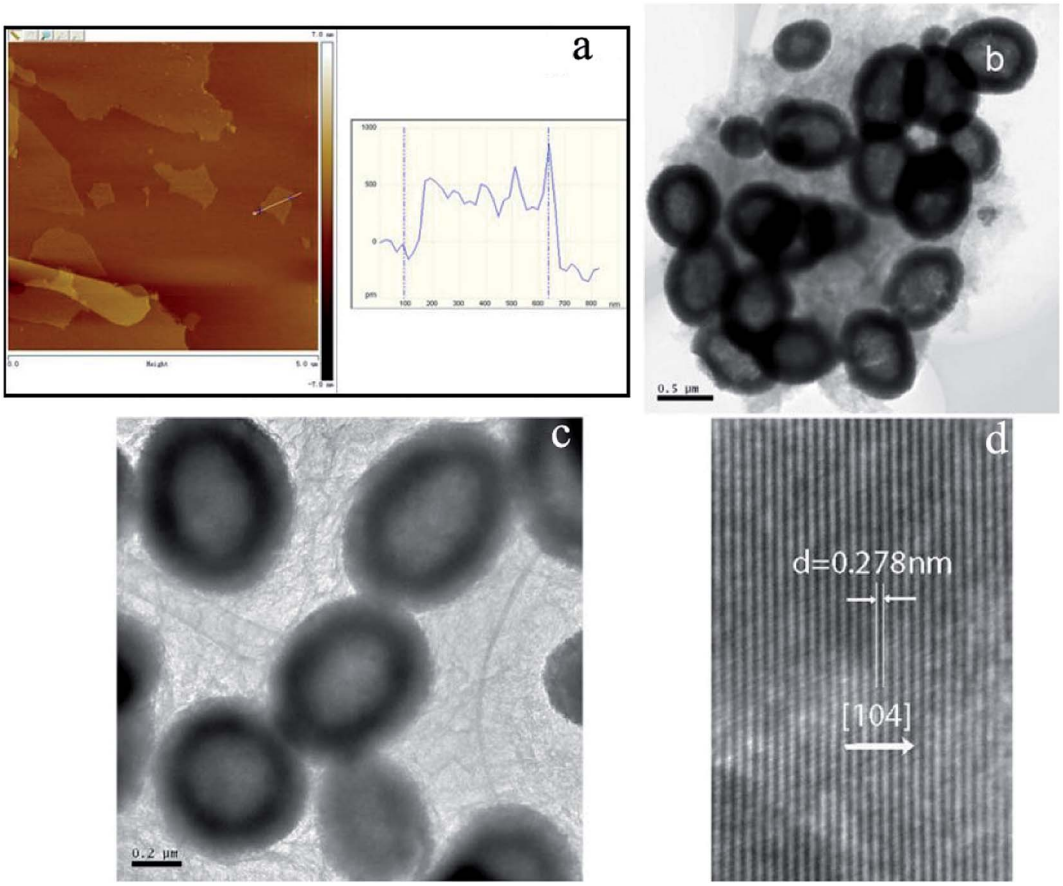

Fig. 2 AFM image of GO (a); TEM images of α-Fe_2O_3/RGO HMM (b, c, and d): (b and c) high magnification, (d) HR-TEM image.

that obtained by using Pt electrode (1.28 Ω cm^2), indicating good electrocatalytic activity of Fe_2O_3/RGO HMM.

The Tafel polarization measurements were employed with the same symmetric cells used for EIS to evaluate the interfacial charge-transfer and the ionic diffusion properties on the electrode surface. As shown in Fig. 5, the intersection of the cathodic branch with the *Y*-axis represents the limiting diffusion current density (J_{lim}), whereas the exchange current density

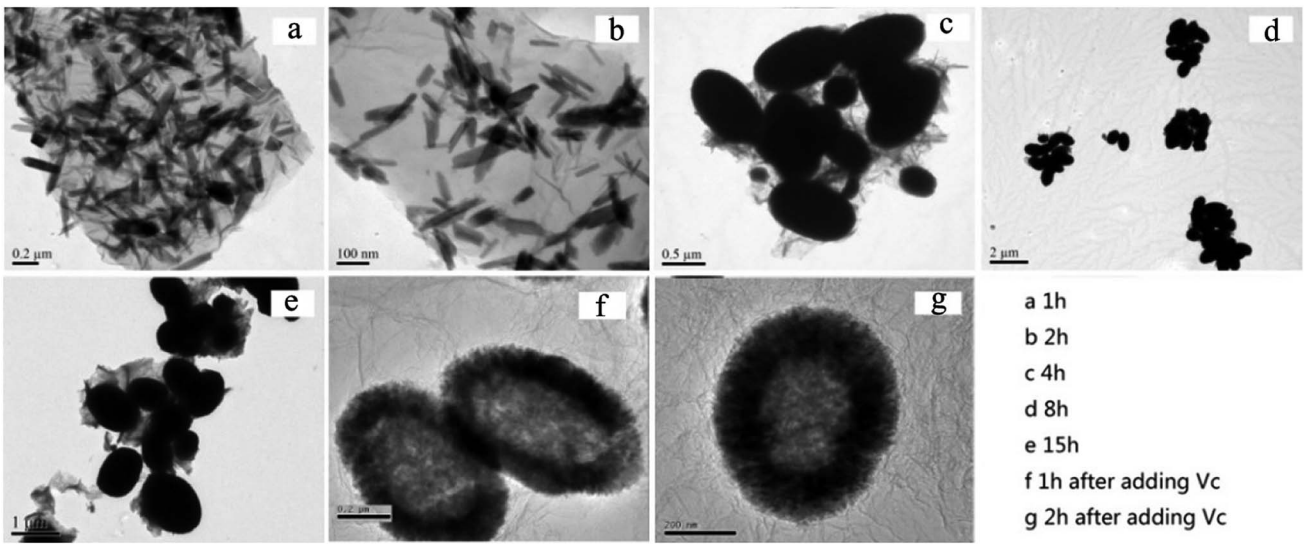

Fig. 3 The TEM images of α-Fe_2O_3/RGO HMM prepared with different synthesis time periods: (a) 1 h, (b) 2 h, (c) 4 h, (d) 8 h, (e) 15 h, and (f) 1 h and (g) 2 h after adding Vc and hexamethylenetetramine.

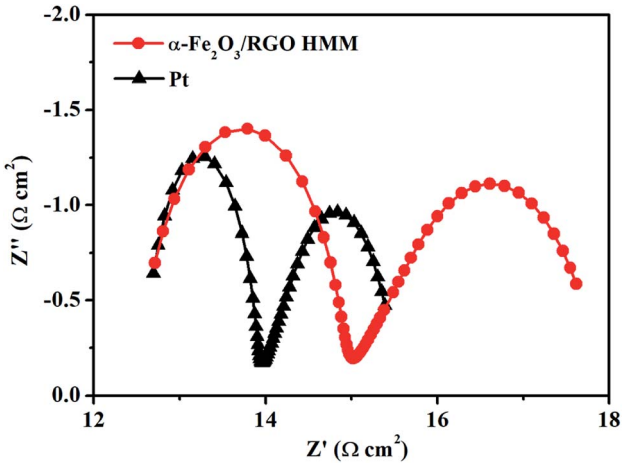

Fig. 4 The Nyquist plots of dummy cells fabricated with α-Fe_2O_3/RGO HMM and Pt electrodes.

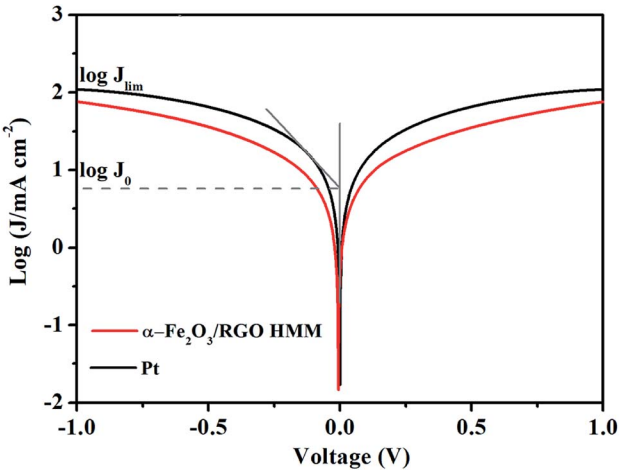

Fig. 5 The Tafel polarization curves of dummy cells fabricated with α-Fe_2O_3/RGO HMM and Pt electrodes.

(J_0) can be obtained from the slope of the cathodic or anodic branch. Further, in the aspect of characterizing the performance of the electrode materials, according to eqn (1) and (2), J_0 indicates the electron-exchange ability and is inversely proportional to R_{ct}, whereas J_{lim} indicates the ionic diffusion coefficient between the two identical electrodes.[26] Consistent with the results of EIS, the J_{lim} and J_0 values of Fe_2O_3/RGO HMM were also found to be close with those of Pt electrode.

$$J_0 = RT/nFR_{ct} \quad (1)$$

$$J_{lim} = 2neDcN_A/l \quad (2)$$

where R is the gas constant, T is the temperature, n is the number of electrons in the reduction of I_3^-, F is the Faraday constant, D is the diffusion coefficient of triiodide, l represents the electrode spacing, C is the concentration of triiodide, and N_A is the Avogadro's constant.

The electrocatalytic activities of α-Fe_2O_3/RGO HMM were further evaluated by cyclic voltammetry (CV) in a three-electrode system at a scan rate of 25 mV s^{-1}. As shown in Fig. 6, α-Fe_2O_3/RGO HMM showed two pairs of reduction and oxidation peaks similar to those for Pt, indicating their same electrocatalytic mechanism toward I_3^- and good reversibility.[39] Further, the relative negative pair corresponds to the redox reaction shown in eqn (3), whereas the positive pair was related to the redox reaction represented in eqn (4) shown below:

$$I_3^- + 2e \leftrightarrow 3I^- \quad (3)$$

$$3I_2 + 2e \leftrightarrow 2I_3^- \quad (4)$$

The peak current densities in lower potential and peak-to-peak separation (E_{pp}) are important parameters to analyze the electrocatalytic properties of CEs. The peak current density was directly proportional to the reduction velocity for reducing I_3^-, and E_{pp} was negatively correlated with the standard electrochemical rate constant.[40] As listed in Table 1, α-Fe_2O_3/RGO HMM gives a larger E_{pp} of 0.37 V than that of Pt CE (E_{pp} = 0.24 V), indicating that α-Fe_2O_3/RGO HMM possesses slower kinetic reduction capability than Pt.[41] However, the peak current density of α-Fe_2O_3/RGO HMM (2.93 mA cm^{-2}) was found to be very close to that of Pt (3.16 mA cm^{-2}), mainly indicating that its structural features were favorable for the electrocatalytic reaction.

The photocurrent density–voltage (J–V) curves of the DSSCs were measured under simulated solar illumination to investigate the photovoltaic properties of the cells with α-Fe_2O_3/RGO HMM and Pt. The corresponding photovoltaic parameters are summarized in a table inserted in Fig. 7. The open-circuit voltage (V_{oc}) was determined by the band position of the photoanode and the electrolyte, and it was observed that the DSSCs based on α-Fe_2O_3/RGO HMM (V_{oc} = 0.73 V) and Pt (V_{oc} = 0.74 V) exhibited the similar V_{oc}. The hollow structure of α-Fe_2O_3 HMM could provide sufficient inner electrocatalytically active sites, in addition to the fast electron transfer channels and improved electrochemical reaction kinetics provided by graphene.[42] Attributed to the combination of the catalytic features of α-Fe_2O_3 HMM and the high conductivity of graphene, α-Fe_2O_3/RGO HMM owns fast electrocatalytic velocity to reduce I_3^- as well as high availability and efficiency of photo-generated electron.

Table 1 EIS, Tafel Polarization, and CV parameters of α-Fe_2O_3/RGO HMM and Pt

CE	R_s (Ω cm^2)	R_{ct} (Ω cm^2)	log J_0 (mA cm^{-2})	log J_{lim} (mA cm^{-2})	E_{pp} (V)
α-Fe_2O_3/RGO HMM	12.72	2.32	0.47	1.87	0.37
Pt	12.70	1.28	0.77	2.04	0.24

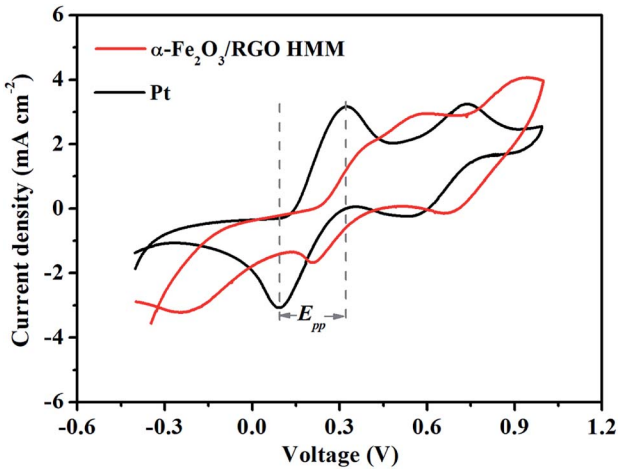

Fig. 6 The cyclic voltammograms of three-electrode system fabricated with α-Fe_2O_3/RGO HMM and Pt electrodes at a scan rate of 25 mV s^{-1}.

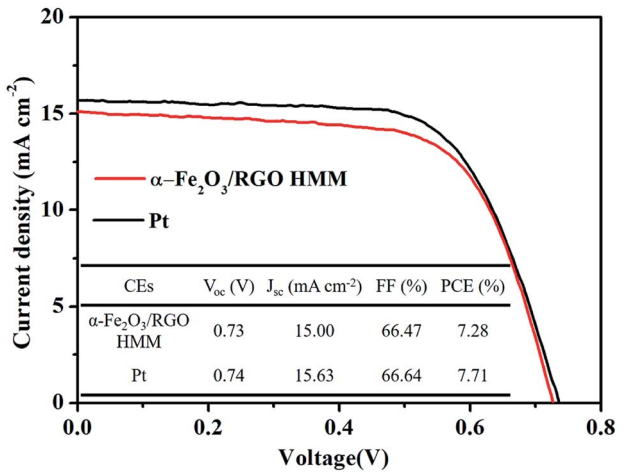

Fig. 7 The photocurrent density–voltage curves of the DSSCs fabricated with α-Fe_2O_3/RGO HMM and Pt.

Reflecting on the photovoltaic parameters, α-Fe_2O_3/RGO HMM exhibited short-current density (J_{SC} = 15.00 mA cm^{-2}) and fill factor (FF = 66.47%), which are comparable with those of the Pt electrode (J_{SC} = 15.63 mA cm^{-2}, FF = 66.64%). Thus, the power conversion efficiency (PCE) of α-Fe_2O_3/RGO HMM reached 7.28%, just slightly inferior to the DSSC based on Pt (7.71%).

4. Conclusions

We adopted the solvothermal treatment to successfully fabricate α-Fe_2O_3 hollow meso–microspheres on graphene sheets with desired size and morphology. As an electroactive material, the α-Fe_2O_3/graphene hollow meso–microspheres provided sufficient inner electrocatalytically active sites and fast electron transfer channels for reducing I_3^- in DSSCs. Our work demonstrates that it is possible to directly grow 0D nanoparticles into 3D hollow mesoporous microspheres on graphene sheets through a one-step solvothermal route under controlled conditions and effectively apply in the water treatment.

Conflicts of interest

There are no conflicts to declare.

References

1 R. B. Lin, Y. He, P. Li, H. Wang, W. Zhou and B. Chen, *Chem. Soc. Rev.*, 2019, **48**, 1362–1389.
2 P. Sudarsanam, E. Peeters, E. V. Makshina, V. I. Parvulescu and B. F. Sels, *Chem. Soc. Rev.*, 2019, **48**, 2366–2421.
3 C. Lethien, J. Le Bideau and T. Brousse, *Energy Environ. Sci.*, 2019, **12**, 96–115.
4 L. Zhang, K. Doyle-Davis and X. Sun, *Energy Environ. Sci.*, 2019, **12**, 492–517.
5 Y. S. Li and J. L. Shi, *Adv. Mater.*, 2014, **26**, 3176–3205.
6 J. Li, Y. W. Wang, W. N. Xu, Y. Wang, B. Zhang, S. Luo, X. Y. Zhou, C. L. Zhang, X. Gu and C. G. Hu, *Nano Energy*, 2019, **57**, 379–387.
7 Q. Zhang, Q. J. Liang, Q. L. Liao, M. Y. Ma, F. F. Gao, X. Zhao, Y. D. Song, L. J. Song, X. C. Xun and Y. Zhang, *Adv. Funct. Mater.*, 2018, **28**, 1803117.
8 C. M. Li, Z. H. Chen, W. Y. Yuan, Q. H. Xu and C. M. Li, *Nanoscale*, 2019, **11**, 1111–1122.
9 Z. X. Wu, W. Li, P. A. Webley and D. Y. Zhao, *Adv. Mater.*, 2012, **24**, 485–491.
10 Y. Hou, D. Wang, X. H. Yang, W. Q. Fang, B. Zhang, H. F. Wang, G. Z. Lu, P. Hu, H. J. Zhao and H. G. Yang, *Nat. Commun.*, 2013, **4**, 1583.
11 F. Jiao, A. Harrison, J. C. Jumas, A. V. Chadwick, W. Kockelmann and P. G. Bruce, *J. Am. Chem. Soc.*, 2006, **128**, 5468–5474.
12 D. Maiti, S. Mukhopadhyay and P. S. Devi, *ACS Sustainable Chem. Eng.*, 2017, **5**, 11255–11267.
13 J. M. Jeong, B. G. Choi, S. C. Lee, K. G. Lee, S. J. Chang, Y. K. Han, Y. B. Lee, H. U. Lee, S. Kwon, G. Lee, C. S. Lee and Y. S. Huh, *Adv. Mater.*, 2013, **25**, 6250–6255.
14 M. Diab and T. Mokari, *Inorg. Chem.*, 2014, **53**, 2304–2309.
15 Y. Zhang, L. Li, W. Ma, Y. Zhang, M. Yu, J. Guo, H. Lu and C. Wang, *ACS Appl. Mater. Interfaces*, 2013, **5**, 614–621.
16 D. Wang, H. Dong, H. Zhang, Y. Zhang, Y. L. Xu, C. J. Zhao, Y. N. Sun and N. Zhou, *ACS Appl. Mater. Interfaces*, 2016, **8**, 19524–19532.
17 S. Mao, G. H. Lu and J. H. Chen, *Nanoscale*, 2015, **7**, 6924–6943.
18 H. Zhang, X. Li, X. Meng, S. Zhou, G. Yang and X. Zhou, *J. Phys.: Condens. Matter*, 2019, **31**, 125301.
19 H. J. Zhang, Y. F. Li, J. H. Hou, K. X. Tu and Z. F. Chen, *J. Am. Chem. Soc.*, 2016, **138**, 5644–5651.
20 J. D. Roy-Mayhew and I. A. Aksay, *Chem. Rev.*, 2014, **114**, 6323–6348.
21 X. Zhang, J. W. Bai, B. Yang, G. Li and L. Liu, *RSC Adv.*, 2016, **6**, 58925–58932.

22 X. Zhang, S. Q. Guo, M. M. Zhen, G. D. Gao and L. Liu, *J. Electrochem. Soc.*, 2015, **162**, 774–779.
23 X. Zhang, Y. X. Yang, S. Q. Guo, F. Z. Hu and L. Liu, *ACS Appl. Mater. Interfaces*, 2015, **7**, 8457–8464.
24 X. Zhang, M. M. Zhen, J. W. Bai, S. W. Jin and L. Lie, *ACS Appl. Mater. Interfaces*, 2016, **8**, 17187–17193.
25 J. X. Yao, K. Zhang, W. Wang, X. Q. Zuo, Q. Yang, H. B. Tang, M. Z. Wu and G. Li, *Nanoscale*, 2018, **10**, 7946–7956.
26 J. X. Yao, K. Zhang, W. Wang, X. Q. Zuo, Q. Yang, H. B. Tang, M. Z. Wu and G. Li, *ACS Appl. Mater. Interfaces*, 2018, **10**, 19564–19572.
27 S. H. Yang, X. F. Song, P. Zhang, J. Sun and L. Gao, *Small*, 2014, **10**, 2270–2279.
28 Z. P. Zhang, H. Y. Zhang, Y. M. Chen, Z. H. Li, Y. Y. Li, T. Luo, Q. B. Wu, Y. W. Xu and C. Y. Zhi, *ChemElectroChem*, 2016, **3**, 1820–1826.
29 S. C. Han, L. F. Hu, Z. Q. Liang, S. Wageh, A. A. Al-Ghamdi, Y. S. Chen and X. S. Fang, *Adv. Funct. Mater.*, 2014, **24**, 5719–5727.
30 A. Manikandan, A. Saravanan, S. A. Antony and M. Bououdina, *J. Nanosci. Nanotechnol.*, 2015, **15**, 4358–4366.
31 Z. Y. Xia, M. Christian, C. Arbizzani, V. Morandi, M. Gazzano, V. Quintano, A. Kovtun and V. Palermo, *Nanoscale*, 2019, **11**, 5265–5273.
32 S. Ren, S. Ma, Y. Yang, Q. Mao and C. Hao, *Electrochim. Acta*, 2015, **178**, 179–189.
33 S. Liu, L. Zheng, P. Yu, S. Han and X. Fang, *Adv. Funct. Mater.*, 2016, **26**, 3331–3339.
34 F. Ye, G. Du, Z. Jiang, Y. Zhong, X. Wang, Q. Cao and J. Z. Jiang, *Nanoscale*, 2012, **4**, 7354–7357.
35 H. Wang, Y. Yang, Y. Liang, L. F. Cui, H. S. Casalongue, Y. Li, G. Hong, Y. Cui and H. Dai, *Angew. Chem.*, 2011, **50**, 7364–7368.
36 C. Z. Wu, P. Yin, X. Zhu, C. Z. OuYang and Y. Xie, *J. Phys. Chem. B*, 2006, **110**, 17806–17812.
37 S. S. Huang, J. T. Zai, D. Ma, Q. Q. He, Y. Y. Liu, Q. Q. Qiao and X. F. Qian, *Chem. Commun.*, 2016, **52**, 10866–10869.
38 C. Xu, Y. Jiang, J. Yang, W. Wu, X. Qian and L. Hou, *Chem. Eng. J.*, 2018, **343**, 86–94.
39 S. S. Huang, D. Ma, Z. J. Hu, Q. Q. He, J. T. Zai, D. Y. Chen, H. Sun, Z. W. Chen, Q. Q. Qao, M. H. Wu and X. F. Qian, *ACS Appl. Mater. Interfaces*, 2017, **9**, 27607–27617.
40 H. M. Li, X. Qian, C. L. Zhu, X. X. Jiang, L. Shao and L. X. Hou, *J. Mater. Chem. A*, 2017, **5**, 4513–4526.
41 F. Du, X. Q. Zuo, Q. Yang, G. Li, Z. L. Ding, M. Z. Wu, Y. Q. Ma and K. R. Zhu, *J. Mater. Chem. C*, 2016, **4**, 10323–10328.
42 H. Yuan, Q. Z. Jiao, J. Liu, X. F. Liu, Y. J. Li, D. X. Shi, Q. Wu, Y. Zhao and H. S. Li, *Carbon*, 2017, **122**, 381–388.